An analysis of wind field estimation and exploitation for quadrotor flight in the urban canopy layer

An Analysis of Wind Field Estimation and Exploitation for Quadrotor Flight in the Urban Canopy Layer

John Ware and Nicholas Roy

***Abstract*— Although unmanned air vehicles' increasing agility and autonomy may soon allow for flight in urban environments, the impact of complex urban wind fields on vehicle flight performance remains unclear. Unlike synoptic winds at high altitudes, urban wind fields are subject to turbulence generated by the buildings and terrain. The resulting spatial and temporal variation makes inference about the global wind field based on local wind measurements difficult and prevents the use of most simple wind models. Fortunately, the structure of the urban environment provides exploitable predictability given a suitable computational fluid dynamics solver, a representative 3D model of the environment, and an estimate of the expected prevailing wind speed and heading. The prevailing wind speed and direction at altitude and computational fluid dynamics solver can generate the corresponding wind field estimate over the map. By generating wind fields in this way, this work investigates a quadrotor's ability to exploit them for improved flight performance. Along with the wind field estimate, an empirically derived power consumption model is used to find minimum-energy trajectories with a planner both aware of and naive to the wind field. When compared to minimum-energy trajectories that do not incorporate wind conditions, the wind-aware trajectories demonstrate reduced flight times, total energy expenditures, and failures due to excess air speed for trajectories across MIT campus.**

I. INTRODUCTION

With unmanned aerial vehicles (UAVs) becoming more prolific and capable, and regulations evolving, their eventual operation in urban environments seems all but certain. As UAVs begin to fly in these environments, they will be presented with a host of unique challenges. One of these challenges will be the complex wind fields generated by urban structures and terrain. Although much effort has been directed towards developing planning and estimation strategies for wind fields at high altitudes or in large open spaces [1]–[7], these approaches contain an implicit assumption that the wind field evolves over relatively large temporal and spatial scales. Given this simplification, a history of local measurements can be used to estimate the global wind field with sufficient accuracy. However, urban wind fields are highly variable in both space and time and are therefore resistant to this estimation method and require an approach that models the complex interaction between the flow and surrounding environment. We seek to show that rotary wing vehicles, such as the quadrotor seen in figure 1, can significantly improve its energy consumption over a trajectory through the urban environment by incorporating the wind field estimate into the planner. Beyond reduced total energy consumption, we also attempt to demonstrate a reduced failure rate and improved time to goal in some instances.

[1]Computer Science and Artificial Intelligence Laboratory (CSAIL), Massachusetts Institute of Technology, Cambridge, MA 02139, USA {jakeware,nickroy}@csail.mit.edu

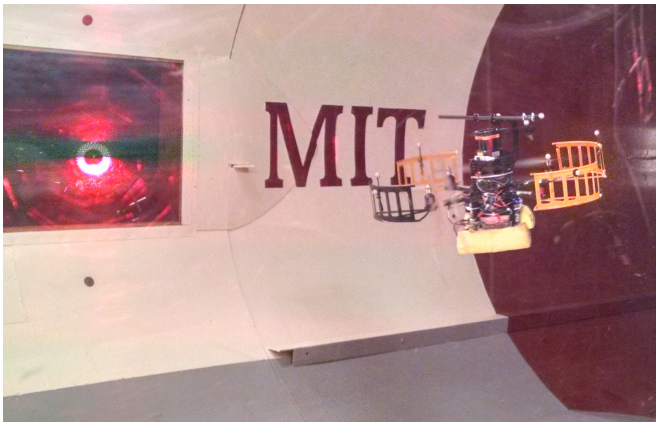

Fig. 1: The quadrotor was flown in the wind tunnel chamber with a Vicon motion capture system in order to measure power consumption as a function of air speed. It executed a position hold command for up to 5 minutes over a range of wind speeds and logged battery voltage and current data, as well as the wind speed within the tunnel.

In order to assess the potential benefits of planning over urban wind fields, this work uses minimum-energy trajectories to characterize the quadrotor's energy consumption between two points with respect to a representative, static wind field within a complex urban environment. An existing computational fluid dynamics (CFD) solver [8] is used to compute the wind field estimates and they are incorporated into a minimum-energy trajectory planner along with an empirically derived quadrotor power consumption model.

This paper proceeds as follows. First, a short summary of related work concerning UAV flight performance in urban environments is presented. This is followed by a summary of the minimum-energy planning problem being solved in order to evaluate the benefit of incorporating urban wind field estimates into quadrotor flight plans. The approach to wind field estimation is then presented along with a validation study of the wind model. This is followed by a discussion of the quadrotor power consumption model, along with a more detailed description of the planning task. Finally, the results from a series of simulations are presented. We also present validations of the power consumption, wind field models, and hover tests of *in situ* measurements, but FAA regulations disallowing urban UAV flights prevent *in situ* validation of the final set of campus-wide flights.

II. RELATED WORK

Three notable efforts have been made to characterize UAV flight in urban environments while using wind models to obtain wind field estimates. Orr et al. [9], [10] used a computational fluid dynamics (CFD) solver to generate static wind fields and assess the waypoint following performance of a fixed-wing UAV. Another effort was made by Galway [11], [12] to simulate an autonomous helicopter in a sparse urban environment. Galway used a CFD model to compute wind fields around cross sections of individual and small groups of buildings for a spanning set of prevailing wind speeds and headings. The resulting library of wind fields was used to construct more complex environments by combining these primitives. Cybyk et al. [13] employed a more sophisticated unsteady wind model for the analysis of fixed wing flight performance in an urban environment with dynamic wind fields. Although Orr et al., Galway, and Cybyk concluded that the resulting wind fields had a significant effect on performance, neither considered the potential benefits of planning over them.

Our approach is similar in that it uses a CFD solver to compute the resulting global wind field given a map of the environment. In contrast to these approaches, the wind model used here will be QUIC-CFD, a lightweight implementation of standard Navier-Stokes based CFD solver capable of generating wind field estimates of large, complex, urban environments. This work also differs in that it focuses on flight within the urban canyon.

III. PLANNING PROBLEM

In order to characterize the potential utility of incorporating urban wind fields into planned trajectories, a method of finding minimum-energy trajectories must first be discussed. Given a map of the environment and a wind field estimate, we seek to efficiently compute the minimum-energy, collision-free trajectory between fixed start and goal locations subject to constraints imposed by the quadrotors capabilities and the operator's notion of safety. In order to minimize energy consumption over the trajectory, our cost function, $C(\cdot)$, is defined as the change in platform energy between two states, χ_i and χ_j. The vehicle state, χ, is defined as the vehicle's xy position and ground velocity, ν_g. The xy position of each state also has a corresponding planar wind vector, $\nu_w(\chi_i)$, from the precomputed wind field estimate[1]. Because we wish to analyze near-terrain flight in the urban environment, we assume the vehicle is flying at a constant altitude close to the ground, and is therefore forced to fly around obstacles rather than over them.

$$C(\chi_i, \chi_{i-1}, \nu_w(\chi_i)) = \Delta E_{tot}(\chi_i, \chi_{i-1}, \nu_w(\chi_i)) \quad (1)$$

Given this cost function and the following set of constraints, the planner attempts to find a trajectory between the fixed start and goal locations that minimizes total energy consumption over some continguous set of edges in the graph leading to the goal.

$$\begin{aligned} \underset{\chi_{0:N}}{\text{argmin}} \quad & \sum_{i=0}^{N} C(\chi_i, \chi_{i-1}, \nu_w(\chi_i)) \\ \text{subject to:} \quad & \nu_{g_{min}} < \nu_{g,i} < \nu_{g_{max}} \\ & \nu_{a,i} < \nu_{a_{max}} \\ & \nu_{g,i} - \nu_{g,i-1} < \nu_{step} \end{aligned} \quad (2)$$

In order to guarantee progress towards the goal and define a window of safe operating speeds, the ground speed, ν_g, is constrained to be greater than 0.5 m/s and less than 8 m/s. The air speed, ν_a, is also subject to a maximum value of either 10 or 20 m/s, representing the vehicle's thrust limits for each set of simulation results. Finally, the instantaneous change in velocity between two adjacent grid points, $\nu_{g,t} - \nu_{g,t-1}$, is constrained to 0.5 m/s. With every iteration, the planner can move in the xy grid along 8 possible headings and can increment or decrement its ground velocity, ν_g, by ν_{step}.

As of yet, we have not discussed an approach to find the energy consumption, $\Delta E_{tot}(\cdot)$, for a quadrotor moving in a known wind field. We also have not shown how to obtain that wind field in a known map of an urban environment in order to provide the planner with an estimate of the wind speed, ν_w, at each location in the map. Although both of these issues are addressed below, the latter will be discussed first for clarity.

IV. URBAN WIND FIELD ESTIMATION

Unlike wind fields found at high altitudes, the dense structure of an urban environment makes wind field estimation a significant challenge. Urban wind fields are largely defined by the aerodynamic boundary layers that form over a city and separate its turbulent interior from the laminar atmospheric flow [14]. The inner-most layer, its height defined by the average height of the terrain features and buildings, is called the urban canopy layer (UCL). Wind fields within the UCL are mostly governed by environmental features which impose a length scale that is often between one and hundreds of meters. Despite the influence of the environmental structure, the general flow pattern in the UCL is still driven by the prevailing wind in the upper boundary layers. Given the strong dependence of the UCL on the conditions in the upper layers, prevailing wind measurements from the roughness sublayer (the next layer in the UCL, just above the roof line) can be used along with a map of the environment, as inputs to a CFD solver. The resulting wind field estimates provide a useful approximation of the wind field created by a given wind condition.

In order for any wind field estimate to be useful for a planner, it must reflect the conditions during the flight. Both work by Van der Hoven [15] and a database of historical wind measurements from the MIT weather station show that although turbulence introduces noise to the prevailing wind conditions, the distribution can be considered stationary over periods of several hours. Given this, trajectory planning can

[1]In this paper, we assume energy is always expended at each time step. Different forms of soaring might allow for energy to be harvested, and would therefore require a different objective, but not fundamentally different strategy to the one we use here.

be done in the wind field corresponding to the expected prevailing wind speed and heading[2]. In this work, we use a set of representative prevailing wind conditions derived from the past year of wind speed and heading data from the MIT weather station.

Fortunately, the structure of a dense urban environment imparts some predictability that can be exploited by a computational fluid dynamics (CFD) solver. For example, wind tends to be channeled down an aligned urban canyon and over a perpendicular one. The most common approach to estimating a wind field in a complex environment is to use CFD solvers to find approximate solutions to the Navier-Stokes equations. This work uses QUIC-CFD, a lightweight CFD solver developed at Los Alamos National Labs. Originally developed to quickly solve for contaminant dispersion in urban environments, it is based on the work of Chorin [16] and uses the steady Reynolds-Averaged Navier-Stokes turbulence model to generate a time-averaged solution. Although QUIC-CFD emphasizes solution time over absolute accuracy, it matched the abiilty of more complex models in its ability to recreate wind conditions at *in-situ* measurement locations during a large field trial in Oklahoma City [17].

Given the guidelines presented by Franke et al. [18] and Tominaga et al. [19], and the solver's inability to vary grid size over the map, the grid size was fixed at 1 m $\times$ 1 m $\times$ 1 m. Further work presented by Oke et al. [20] informs the selection of map size. Given the dimensions and spacing of buildings, the incoming flow regime is considered to be skimming flow and predicts little disturbance by the urban canyons. The boundary conditions are the Monin-Obukhov, logarithmic boundary conditions found in Oke [20] with neutral stability.

Figure 2 shows the x-component of the velocity for a representative wind field generated with a 10 m/s wind speed measured at 100 m and an Easterly wind heading of 90 degrees. Note the higher wind speeds in the aligned canyons and wake regions behind structures.

V. CFD MODEL VALIDATION

To validate our wind model, a series of *in situ* wind speed and heading measurements were taken with a LCJ Capteurs CV7 ultrasonic anemometer at an altitude of 2 meters and a rate of 4 Hz. Each measurement period was approximately 20 minutes, and all measurements were done within a 2 hour period. The prevailing wind was measured to have an average speed and heading of 2.9 m/s at 100 m and 102 degrees, respectively, and was compared against a steady wind field generated using QUIC-CFD with a prevailing wind speed of 5 m/s at 100 m and a heading of 90 degrees. The measurement locations can be seen in figure 3.

A table of the average anemometer and model speed, S, and average anemometer and model heading, Θ, can be seen in table I. The heading values are in the standard meteorological form of degrees North with clockwise as

[2]In our model, turbulence is a form of uncertainty, along with other possible sources of uncertainty. Incorporating uncertainty in general may further improve performance, but is outside the scope of this paper.

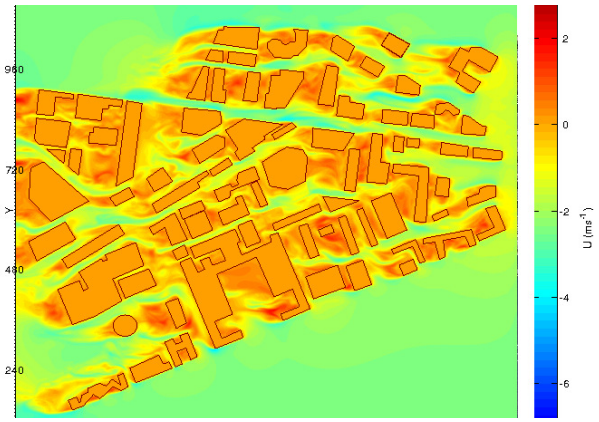

Fig. 2: A visualization of the x-component of the velocity in a planar slice of the three-dimensional wind field for a prevailing wind speed of 10 m/s measured at an altitude of 100 m and a prevailing wind heading of 90 degrees.

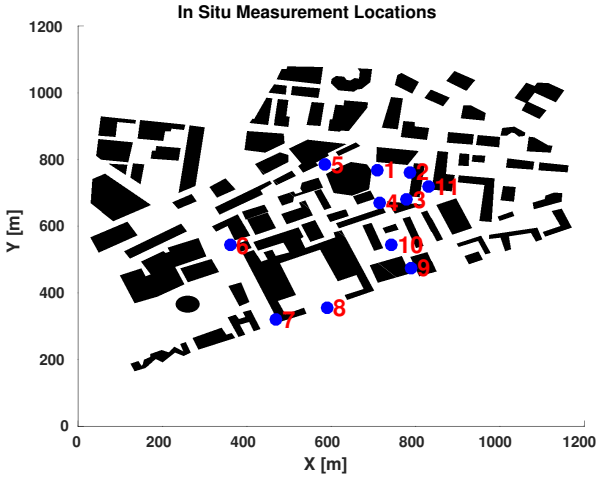

Fig. 3: *In situ* measurement locations across MIT campus. The measurements were taken over the course of 2 hours with an ultrasonic anemometer.

positive. Note also that heading refers to the source of the wind, and not to the direction of flow. To account for uncertainty in the test location, the model average was computed over a 5 m $\times$ 5 m area. So as to value the model's ability to capture the bulk advection effect over its ability to recreate a particular flow feature at a specific position, the measurement location was adjusted within several meters for a more favorable comparison. Given these allowances, the model performs similarly to the results shown in [8], with approximately 36% of measurement locations showing wind heading errors of less than 15 degrees, and 72% less than 45 degrees. Approximately 36% of measurement locations show wind speed errors of less than 10%, and 81% show wind speed errors of less than 50%. Also, the magnitudes of the speed error's standard deviation suggests that our ground velocity, ν_g, discretization of 0.5 m/s was appropriate. Although the magnitudes of the heading error's standard deviation are large, this is to be expected in the turbulent urban canyon and reinforces the approach of planning over the expected wind conditions.

TABLE I: Measured and Model Wind Speed and Heading

Point	Measured		Model		Mean Error		Std. Dev. Error	
	S	Θ	S	Θ	μ_S	μ_θ	σ_S	σ_θ
1	1.17	207	1.26	220	-0.09	-13	0.62	37
2	1.52	346	1.11	317	0.41	29	0.52	24
3	1.68	96	1.54	101	0.14	-5	0.60	11
4	1.08	65	1.24	37	-0.16	28	0.56	39
5	0.94	293	0.90	289	0.03	4	0.36	18
6	0.87	44	0.81	93	0.06	-50	0.30	26
7	1.01	11	0.77	339	0.24	72	0.27	15
8	1.11	29	0.78	127	0.33	-99	0.43	17
9	0.86	198	0.61	158	0.25	40	0.24	15
10	0.58	232	1.33	211	-0.75	21	0.37	103
11	0.87	196	1.53	203	-0.65	-7	0.31	40

All speed values are in m/s and heading values are in degrees north.

VI. ENERGY CONSUMPTION

In order to find a minimum energy trajectory, it is necessary to compute the quadrotor's energy consumption between two points in the map. We can express the vehicle's total energy, E_{tot}, as the sum of the potential, kinetic, and stored energy as shown in equation 3. The stored energy component, E_s, represents the capacity in J of the on-board battery,

$$E_{tot} = mgh + \frac{1}{2}m|\nu|^2 + E_s. \tag{3}$$

Assuming a constant ground velocity, constant altitude, and no acceleration, the change in total energy, ΔE_{tot}, is equal to the change in stored energy, ΔE_s. The change in stored energy is the difference in the battery's stored energy between two points in time. Note also that we will later assume no acceleration between nodes in the planning graph.

For a rotary wing vehicle, and especially a quadrotor, the act of spinning the rotors consumes the vast majority of the stored energy and a power consumption model of the controller, motor, and rotor system is required. Huang et al. [21] express the power consumption, P, of a single rotor as a function of induced velocity (ν_i), air speed (ν_∞), rotor thrust (T), angle of attack (α), propeller efficiency (η_p), motor efficiency (η_m), and controller efficiency (η_c). The efficiencies are taken to be 0.6, 0.85, and 0.95, respectively.

$$P = \frac{T(\nu_i - \nu_\infty \sin\alpha)}{\eta_p \eta_m \eta_c} \tag{4}$$

The induced velocity is the rate at which the motion of the rotor moves air perpendicular to the rotor plane. Note that this power model depends not on air velocity but on induced velocity which is not directly measured, but requires solving the quadratic expression found in equation 5. Here, the free stream velocity, ν_∞, is equivalent to the airspeed of the vehicle, ν_a. The hover velocity, ν_h, is defined in equation 6 with the hover thrust, T_h, equal to $1/4$ of the vehicle weight, S as the swept rotor area, and ρ as the air density.

$$\nu_i = \frac{\nu_h^2}{\sqrt{(\nu_\infty \cos\alpha)^2 + (\nu_i - \nu_\infty \sin\alpha)^2}} \tag{5}$$

$$\nu_h = \sqrt{\frac{T_h}{2\rho S}} \tag{6}$$

Instead of mounting the vehicle on a sting in the wind tunnel and introducing significant measurement noise into the force and moment sensors a motion capture system was setup within the MIT Wright Brothers Wind Tunnel and the vehicle was flown in place, as shown in figure 1. The vehicle maintained position while the air speed was set and held at 5, 10, 15, 20, and 25 mph for durations between 30 seconds and several minutes. A series of 11, constant air speed tests were performed over the course of several days. The vehicle's battery voltage and current were measured at 1 kHz, averaged, and recorded at 100 Hz. The wind speed was closely controlled and recorded at 4 Hz by a LCJ Capteurs CV7 ultrasonic anemometer.

The resulting calculated power consumption and measured power consumption data, normalized by the hover power consumption, P_h, of 247 W, can be seen in figure 4. To validate the measured power consumption data, a curve was fit to the average pitch values for all trials to serve as an input to equations 4 and 5. The measured pitch data and quadratic curve fit can be seen in panel figure 4(a). The output of this power consumption model, given the fit of pitch as a function of air speed, can be seen, along with the measured power consumption, in figure 4(b). Note the initial decrease in power consumption caused by translational lift and the steep increase at higher air speeds caused primarily by the vehicles angle of attack and form drag. Translational lift is present in all rotorcraft and is a natural result of the increased flow over the rotors in forward flight which improves rotor efficiency [22]. The discrepancy between the measured power consumption and the calculated power consumption is probably due to a combination of imperfect modeling of the controller, motor, and rotor efficiencies and the vehicles difficulty holding position at the higher air speeds due to controller constraints.

A series of outdoor hover tests were performed to compare the quadrotor's energy consumption in the field to the controlled tests from the wind tunnel. In order to comply with FAA regulation, the tests were done on the test frame seen in figure 5. The wind speed was recorded with a Young 81000 ultrasonic anemometer and the vehicle's battery voltage and current consumption were logged. Because multipath error and obstruction of the horizon prevented accurate localization with GPS, a downward facing optical flow camera, the 3DR PX4Flow, was used instead. The magnetometer was used for the vehicle's yaw orientation. Although the resulting power consumption data does capture the downward trend, it is likely that large deviations in the control effort due to turbulence cause a back EMF current to the battery that degrades the measurement accuracy.

VII. PLANNING

Given a planar section of the 3D wind field estimate and occupancy map, A* search was used to find the minimum-cost, collision-free trajectory between a start and goal location over xy positions and scalar edge velocity. A velocity discretization of 0.5 m/s allowed for sufficiently fine adjustment of the ground velocity. The vehicle's altitude was

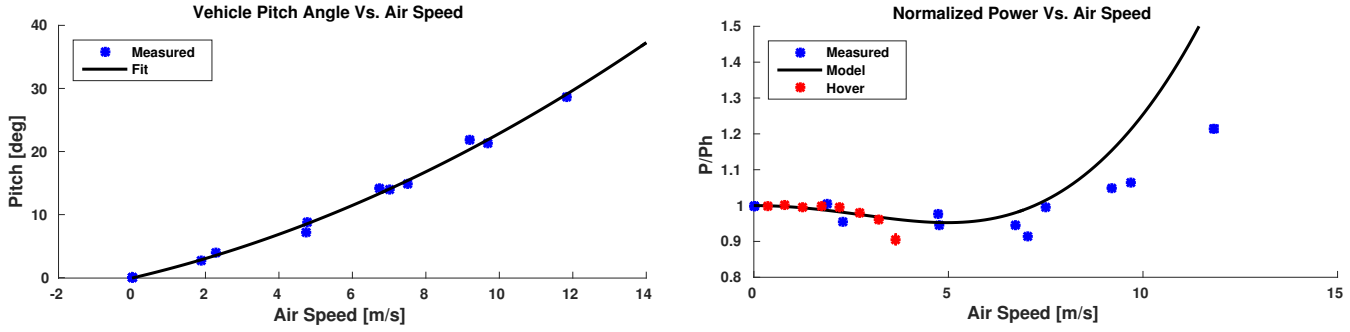

(a) (b)

Fig. 4: Panel (a) shows the mean and standard error of the vehicle pitch along with a quadratic fit to the data. These values were used to generate the power consumption model, shown in black, in panel (b). Power consumption data was normalized by the hover power consumption in still air. The blue points denote the results as reported by the current and voltage sensor with the associated standard error. The red points denote the power consumption during the outdoor hover tests and their standard error. Note that the standard error for the wind tunnel trials is negligible due to sampling frequency and test duration.

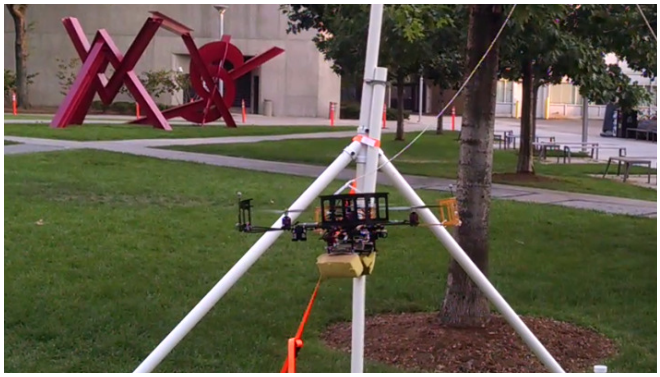

Fig. 5: A series of hover tests were performed in a green space within the MIT campus. The vehicle was autonomously holding position, but tethered to comply with FAA regulations.

fixed to 10 meters and the planning was performed directly on the xy grid used by the wind model. The vehicle's air speed was calculated as the ground speed minus the wind speed. To find the stored energy consumption between two states, power consumption as a function of air speed is multiplied by the edge distance and divided by the current ground speed. Recall that our model of urban operations only considers motion at a fixed altitude in the xy-plane, the energy consumed between two states, χ_i and χ_j, can then be expressed as follows with $dist(\chi_i, \chi_j)$ as the Euclidean distance function between two nodes and ν_g as the vehicle ground speed along the connecting edge.

$$\Delta E_{tot}(\chi_i, \chi_{i-1}j, \nu_g(\chi_i)) = \frac{P(\nu_{g,i} - \nu_{w,i})dist(\chi_i, \chi_{i-1})}{\nu_{g,i}} \tag{7}$$

Two sample sets of 1000 simulated, minimum-energy trajectories using 500 random start and goal locations were planned with both the naive and wind-aware planners. In order to demonstrate the effect of constraining the vehicle's maximum air speed, the two sets of simulations had max air speeds of 10 and 20 m/s, respectively. The minimum distance between the start and goal locations was 10 m and the 10 wind conditions were comprised of 5 speeds and 2 headings. In order to represent the vehicles flight envelope, failure is defined as the case when the planner is unable to lower its ground speed sufficiently to prevent exceeding the maximum air speed, while still making forward progress.

To allow for sufficiently long trajectories, a region of the MIT campus and surrounding city spanning an area of 1100 m $\times$ 1100 m was selected. A three-dimensional model of this region containing 81 buildings, each constrained to be no taller than 20 m, was created to serve as an input to the wind model and can be seen in figure 6. The domain height, the maximum height of the model's air volume, was constrained to 24 m to minimize computation time and a xyz-grid resolution of 1 m $\times$ 1 m $\times$ 1 m was used to capture the detailed structure of UCL wind fields. Despite only planning in the plane, the wind model must solve over the full 3D map to account for the complex flow through the urban environment. Although constraining the domain and building height makes for an imperfect model, the focus of this work was on flight within the urban canyon, and *in situ* measurements demonstrate that the resulting wind fields remain sufficiently accurate.

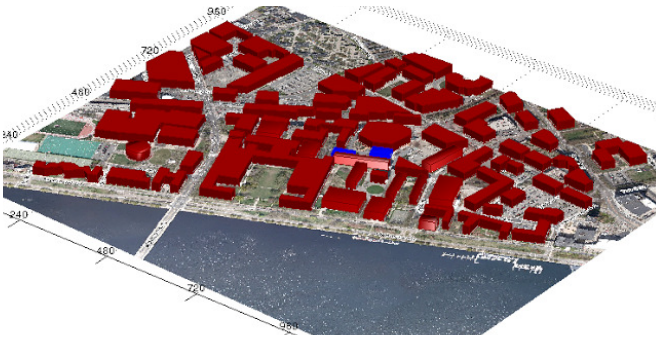

Fig. 6: The 3D model of the region of MIT campus being planned over that was used as an input to the QUIC-CFD wind model along with the prevailing wind conditions.

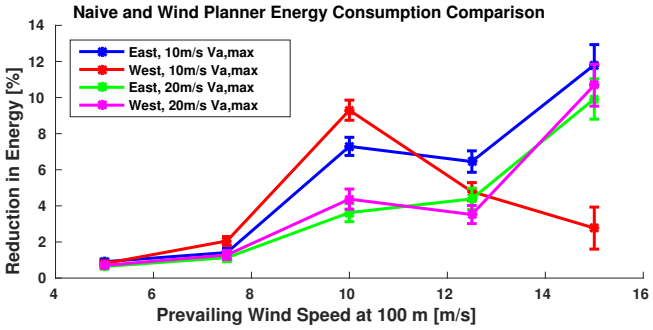

Fig. 7: The wind planner significantly outperforms the naive planner over all prevailing wind speeds tested. The error bars shown here represent standard error.

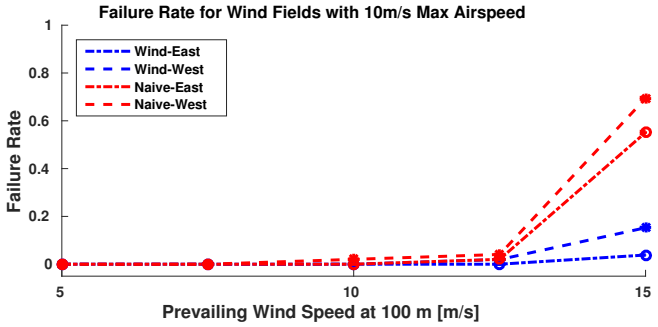

Fig. 8: Neither planner has significant error rates below 12.5 m/s, but the naive planner strongly underperforms the wind planner for a 15 m/s prevailing wind speed. The error bars shown here represent standard error.

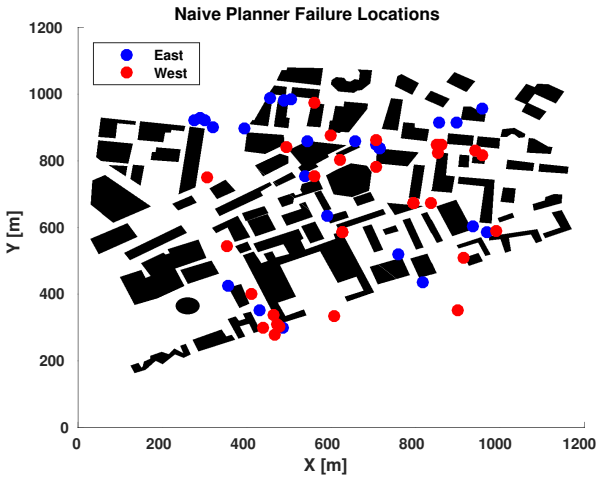

Fig. 9: The naive planner failure locations over the 2D map. Note that a large fraction of them are at corners of buildings or at the entry points to the structure group near canyons channeling the wind along their axis.

As a coastal city, Cambridge typically has either an Easterly or Westerly wind heading and might only switch once a day due to the diurnal cycle. With this in mind, wind fields with both an Easterly and Westerly wind heading were used here with wind speeds of 5, 7.5, 10, 12.5, and 15 m/s for a total of 10 wind fields. Given the past year of data from the MIT weather station, these wind speeds occur in approximately 27%, 11%, 3.5%, 1.3%, and 0.35% of the measurements, respectively. A visualization of one of these wind fields can be seen in figure 2. The resulting trajectories are used to draw more general conclusions about the benefits of wind-aware planning in the urban environment.

VIII. RESULTS

A good comparison metric between the two planners is the mean percentage difference in energy consumption. This is shown in figure 7 for both maximum air speeds over each of the 10 wind fields across all 500 trials. For the simulations with the 20 m/s maximum air speed, the wind planner, as might be expected, outperforms the naive planner over all wind conditions and is able to improve its performance with increasing wind speed. Because a prevailing wind speed of 5 m/s at an altitude of 100 m generates relatively small wind speeds at an altitude of 10 m, the wind planner is only able to reduce energy consumption by approximately 0.5%. Although there is only a small change at 7.5 m/s, the wind planner's performance increases significantly with increasing prevailing wind speed and acheives approximately a 4%, and 10% improvement at 10, and 15 m/s, respectively. This is likely because it is able to exploit tail winds, while the naive planner unknowingly flies into headwinds.

The second set of simulations used a maximum air speed of 10 m/s and resulted in a change in the wind planner performance. Again, the wind planner significantly outperforms the naive planner in all cases, and is only able to reduce energy consumption by approximately 0.9% for a prevailing wind speed of 5 m/s. Demonstrating the additional expense incurred by the naive planner's upwind trajectories, relatively large gains of 7.3% and 9.3% are shown at 10 m/s for the Easterly and Westerly wind headings, respectively. As might be expected, the wind planner shows equivalent or increased gains for 12.5 and 15 m/s in the Easterly wind fields. Surprisingly, the energy consumption decreases for the Westerly heading. This may be due to the Westerly wind being channeled down the aligned urban canyons and causing otherwise costly upwind trajectories to fail. Some evidence of this failure mode can be found in figure 9 by noting the cluster of naive planner failures for the Westerly wind heading at the lower left of the map leading into a large diagonal canyon. Also note that the naive planner fails to reach the goal location in approximately 55% and 69% of the 15m/s trials, as shown in figure 8. These incomplete trials cannot be counted towards the mean energy consumption, but would likely be some of the highest values in the set.

Looking closer at a specific trial, figure 10 (a) and 10 (b) show the total energy consumption and speeds over the length of the trajectory for a wind speed of 10 m/s and Westerly heading. By maximizing its ground speed without exceeding the maximum air speed, the wind planner demonstrates a 39.4% reduction in total energy consumption while traveling 10.8% further with a 22% shorter flight time. The resulting trajectories in figure 11 show the wind planner sheltering next to and downwind from structures, while the naive planner exposes the vehicle to a strong headwind.

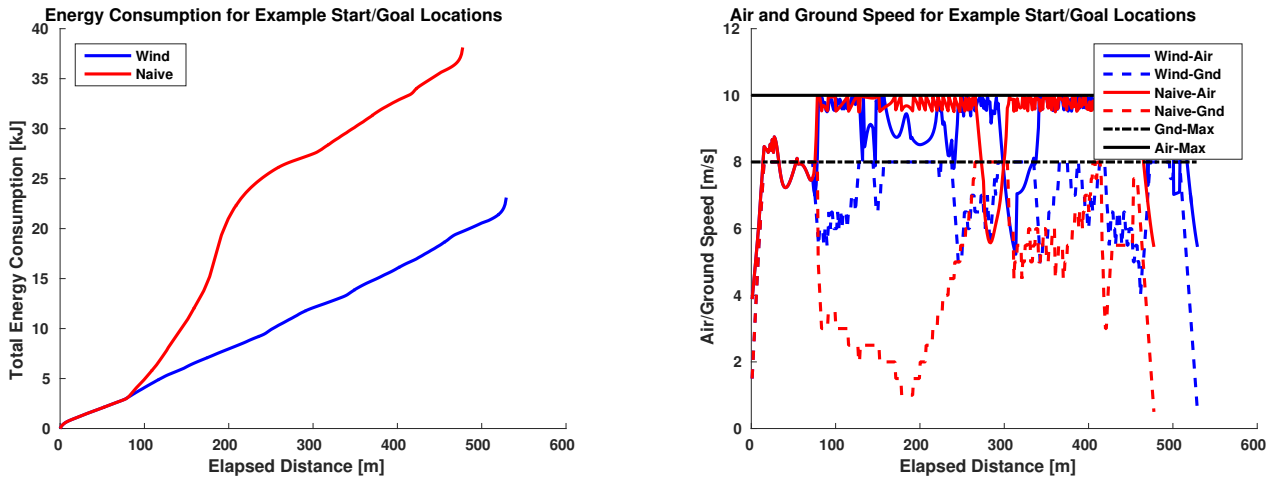

(a) (b)

Fig. 10: Panel (a) demonstrates the wind planner's ability to reduce energy consumption over the course of a flight. Panel (b) shows how the naive planner is unable to increase its ground speed due to its own dynamic constraints and the upwind, exposed trajectory it selected.

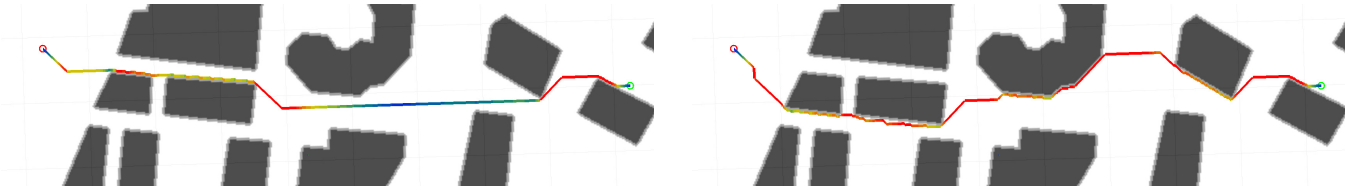

(a) (b)

Fig. 11: Panel (a) and (b) show the naive and wind planner's trajectories, respectively, for an example start and goal location. The trajectories are color coded by ground speed. The green and red circles denote the start and goal locations, respectively.

IX. CONCLUSIONS AND FUTURE WORK

Although the lower wind speeds offer little opportunity for exploitation within a dense urban environment, those above 10 m/s allowed the wind planner to significantly outperform the naive planner. Given a complex urban environment with a wind field estimate, the planner is capable of finding minimum-energy trajectories such that the vehicle is less likely to exceed its flight performance envelope given strong headwinds and more likely to exploit tailwinds for a reduced time to goal and total energy consumption. More generally, this initial investigation suggests that UAVs could benefit from considering wind conditions in complex environments. Future work will focus on leveraging unsteady wind models, integrating high frequency prevailing wind updates for online re-planning, and integrating uncertainty estimates in to the wind field representation.

REFERENCES

[1] M. J. Allen and V. Lin, "Guidance and control of an autonomous soaring uav," in *NASA Technical Memorandum*, 2007.

[2] J. W. Langelaan, J. Spletzer, C. Montella, and J. Grenestedt, "Wind field estimation for autonomous dynamic soaring," in *IEEE Internation Conference on Robotics and Automation*, 2012.

[3] Y. J. Zhao and Y. C. Qi, "Minimum fuel powered dynamic soaring of unmanned aerial vehicles utilizing wind gradients," in *Optimal control applications and methods*, 2004.

[4] N. Lawrance and S. Sukkarieh, "Simultaneous exploration and exploitation of a wind field for a small gliding uav," in *AIAA Guidance, Navigation, and Control Conference*, 2010.

[5] ——, "Autonomous exploration of a wind field with a gliding aircraft," in *Journal of Guidance, Control, and Dynamics*, 2011.

[6] ——, "Path planning for autonomous soaring flight in dynamic wind fields," in *IEEE International Conference on Robotics and Automation*, 2011.

[7] A. Chakrabarty and J. Langelaan, "Uav flight path planning in time varying complex wind-fields," in *American Control Conference*, 2013.

[8] A. A. Gowardhan, E. R. Pardyjak, I. Senocak, and M. J. Brown, "A cfd-based wind solver for an urban

fast response transport and dispersion model," in *Environmental fluid mechanics*, 2011.

[9] M. W. Orr, S. J. Rasmussen, E. D. Karni, and W. B. Blake, "Framework for developing and evaluating mav control algorithms in a realistic urban setting," in *American Control Conference*, 2005.

[10] D. Gross, S. Rasmussen, P. Chandler, and G. Feitshans, "Cooperative operations in urban terrain (counter)," in *Defense and Security Symposium*, 2006.

[11] D. Galway, J Etele, and G. Fusina, "Modeling of urban wind field effects on unmanned rotorcraft flight," in *Journal of Aircraft*, 2011.

[12] ——, "Development and implementation of an urban wind field database for aircraft flight simulation," in *Journal of Wind Engineering and Industrial Aerodynamics*, 2012.

[13] B. Cybyk, B. McGrath, T. Frey, D. Drewry, J. Keane, and G Patnaik, "Unsteady airflows and their impact on small unmanned air systems in urban environments," in *Journal of Aerospace Information Systems*, 2014.

[14] T. R. Oke, *Urban Environments*. McGill–Queens University Press, 1997.

[15] I. Van der Hoven, "Power spectrum of horizontal wind speed in the frequency range from 0.0007 to 900 cycles per hour," in *Journal of Meteorology*, 1957.

[16] A. J. Chorin, "A numerical method for solving incompressible viscous flow problems," in *Journal of computational physics*, 1967.

[17] M. Neophytou, A. Gowardhan, and M. Brown, "An inter-comparison of three urban wind models using oklahoma city joint urban 2003 wind field measurements," in *Journal of Wind Engineering and Industrial Aerodynamics*, 2011.

[18] J. Franke, A. Hellsten, K. H. Schlunzen, and B. Carissimo, "The cost 732 best practice guideline for cfd simulation of flows in the urban environment: a summary," in *International Journal of Environment and Pollution*, 2011.

[19] Y. Tominaga, A. Mochida, R. Yoshie, H. Kataoka, T. Nozu, M. Yoshikawa, and T. Shirasawa, "Aij guidelines for practical applications of cfd to pedestrian wind environment around buildings," in *Journal of wind engineering and industrial aerodynamics*, 2008.

[20] T. R. Oke, "Street design and urban canopy layer climate," in *Energy and buildings*, 1988.

[21] H. Huang, G. M. Hoffmann, S. L. Waslander, and C. J. Tomlin, "Aerodynamics and control of autonomous quadrotor helicopters in aggressive maneuvering," in *IEEE Internation Conference on Robotics and Automation*, 2009.

[22] J. G. Leishman, *Principles of Helicopter Aerodynamics with CD Extra*. Cambridge university press, 2006.